Materials and Design 36 (2012) 337–347

Contents lists available at SciVerse ScienceDirect

Materials and Design

journal homepage: www.elsevier.com/locate/matdes

Thermal aging effects on the microstructure of Nb-bearing nickel based superalloy weld overlays using ultrasound techniques

Victor Hugo C. de Albuquerque [a], Cleiton Carvalho Silva [b], Paulo G. Normando [b], Elineudo P. Moura [b], João Manuel R.S. Tavares [c,*]

[a] Universidade de Fortaleza, Centro de Ciências Tecnológicas, Avenida Washington Soares, 1321, CEP 60.811-905, Edson Queiroz, Fortaleza, Ceará, Brazil
[b] Universidade Federal do Ceará, Departamento de Engenharia Metalúrgica e de Materiais, Bloco 714, CEP 60455-760, Campus do Pici, Fortaleza, Ceará, Brazil
[c] Instituto de Engenharia Mecânica e Gestão Industrial & Departamento de Engenharia Mecânica, Faculdade de Engenharia, Universidade do Porto, Rua Dr. Roberto Frias, S/N – 4200-465 Porto, Portugal

ARTICLE INFO

Article history:
Received 27 October 2011
Accepted 15 November 2011
Available online 25 November 2011

Keywords:
F. Microstructure
G. Nondestructive testing (NDT)
G. Ultrasonic analysis

ABSTRACT

Secondary phases such as Laves and carbides are formed during the final stages of solidification of the nickel based superalloy Inconel 625 coatings deposited during the gas tungsten arc welding (GTAW) cold wire process. However, when aged at high temperatures, other phases can precipitate in the microstructure, like the γ'' and δ phases. The aim of this work was to evaluate the different phases formed during thermal aging of the as-welded material through ultrasound inspection, as well as the influence of background echo and backscattered ultrasound signals on the computational classification of the microstructures involved. The experimental conditions employed an aging temperature of 650 °C for 10, 100 and 200 h. The ultrasound signals were acquired using transducers with frequencies of 4 and 5 MHz and then processed to determine the ultrasound velocity and attenuation, as well as to study the background echo and backscattered signals produced by wave propagation. Both signal types were used to study the effectiveness and speed for classifying the secondary phases, using detrended fluctuation analysis and the Hurst method in the signal pre-processing and the Karhunen–Loève Transform in the classification of the microstructures. The ultrasound signals and the signal processing tools used were considered sufficiently sensitive, fast and accurate in the detection and classification of the microstructures in the as-welded and aged Inconel 625 alloy using this nondestructive technique.

1. Introduction

Nb-bearing nickel-based superalloys, like the Inconel 625 alloy, exhibit an outstanding combination of mechanical properties and resistance to pitting, crevice and intergranular corrosion due to the stiffening effect of chromium, molybdenum and niobium on its nickel matrix, making precipitation-hardening treatments unnecessary [1]. The extraordinary resistant against a wide range of organic and mineral acids is due to their excellent anti-corrosive properties, manly, at high temperatures. These alloys are commonly found in the marine, aerospace, chemical and oil and gas industries [2–4].

In particularly, the Inconel 625 alloy has greater applicability, especially in highly corrosive environments such as the oil and gas industry, than many other Ni-base alloys. Nowadays, this alloy is widely used in the weld overlay of the inner surface of carbon steel pipes and other equipment for offshore applications. However further studies of this alloy such as the one reported in this paper are required to increase the overall knowledge concerning its properties.

During welding with the Inconel 625 alloy, there is intensive microsegregation of elements, such as niobium and molybdenum, within the interdendritic regions causing the supersaturation of the liquid metal in its final stage of solidification, which results in the precipitation of Nb-rich Laves phase and MC primary carbides type NbC [5,6]. The segregation and precipitation of the secondary phases can change the mechanical properties of the alloy and decrease its resistance to corrosion [7]. In addition, the Nb-rich Laves phase has a low melting point that causes an increase in the temperature solidification range, making the alloy susceptible to solidification cracking [8]. However, an adequate selection of the welding conditions can minimize the formation of the Nb-rich Laves phases thus reducing susceptible to solidification cracking. Also it is important to investigate the phase transformation process.

Although there are important and numerous engineering uses for Inconel 625 alloy, knowledge concerning its properties is still very scarce and consequently much research has been carried

* Corresponding author. Tel.: +351 22 5081487; fax: +351 22 5081445.
E-mail addresses: victor.albuquerque@fe.up.pt (Victor Hugo C. de Albuquerque), cleitonufc@yahoo.com.br (C.C. Silva), paulo.garcia@metalmat.ufc.br (P.G. Normando), elineudo@ufc.br (E.P. Moura), tavares@fe.up.pt (João Manuel R.S. Tavares).

0261-3069/$ - see front matter © 2011 Elsevier Ltd. All rights reserved.
doi:10.1016/j.matdes.2011.11.035

out on this alloy. For example, Evans et al. [9] studied foil and sheet forms of the Inconel 625 alloy in as-processed condition and following creep-rupture testing in air at 750 °C and 100 MPa. Mathew et al. [10] evaluated the effect of aging, for 500 h at six different temperatures in the range of 873–1173 K, on the mechanical behavior of the Inconel 625 alloy using a nondestructive stress/strain microprobe system. Zhang et al. [11] investigated the Inconel 625 alloy thermally sprayed using high velocity oxy-fuel process. The coatings deposited by a liquid-fuelled gun were compared with the ones produced by a gas-fuelled system. The microstructural evolution of the coatings was accomplished using scanning electron microscopy and X-ray diffraction. Ganesh et al. [12] analyzed the fatigue crack growth and fracture toughness characteristics of an Inconel 625 laser rapid manufactured alloy. Cooper et al. [13] verified the seawater corrosion behavior of three Inconel 625 alloy laser processed surfaces: (i) one produced by laser melting, and the other two by (ii) laser melt/particle injection processing with tungsten carbide (WC) and (iii) with titanium carbide (TiC) particles. Arafin et al. [14] investigated a combination of experimental and computational techniques to predict the time required to complete isothermal solidification during the transient liquid phase bonding of the Inconel 625 alloy. Mathew et al. [15] evaluated the creep rupture properties of the same alloy when service-exposed for 60,000 h at 720 °C. The creep tests were carried out at various temperatures between 650 and 900 °C, and the rupture times varied up to 32,000 h. Song and Nakata [16] evaluated the mechanical properties of friction stir welded and post-heat-treated Inconel 625 alloy through friction stir welding rotation and traveling speeds of 200 rpm and 100 mm/min, respectively; heat treatment was carried out after welding at 700 °C for 100 h in vacuum. Li et al. [17] studied hot compressions tests of an Inconel 625 superalloy using the Gleeble-1500 simulator (Dynamic Systems Inc., USA) and adopting different strains between 900 and 1200 °C and a strain rate of 0.1 s^{-1}. Optical microscope, transmission electron microscope and electron backscatter diffraction technique were employed to investigate the microstructure evolution and nucleation mechanisms of dynamic recrystallization.

A detailed review about various types of nickel-based alloys available on a commercial basis and their development, including alloying additions as well as processing techniques used to achieve specific mechanical and/or chemical properties, can be seen in [18].

Nondestructive tests, predominantly ultrasonic methods, have been used on Inconel 625 alloy to provide more efficient and accurate studies. These methods have been used to investigate the long term service degradation of this alloy in cracker tubes of heavy water plants [19]. The effect of aging on the mechanical behavior of the alloy at six different temperatures (from 600 to 900 °C) over 500 h was investigated using an automated ball indentation technique. The technique demonstrated its effectiveness to detect changes in the mechanical properties due to aging [10]. Another investigation into the influence of thermal aging from 650 to 950 °C on the same alloy using ultrasonic velocity measurements to characterize the microstructures correlated to the tensile properties and hardness, which were determined using ball indentation technique, was reported in [20].

The velocity and attenuation of ultrasonic waves have been widely used for several decades to determine mechanical properties of solids in an accurate, fast and nondestructive manner. The interaction between ultrasonic measurements and microstructures can be evaluated through background echo and backscattered signals [21–23]. Therefore, the main goal of this work is to evaluate the sensitivity of ultrasound measurements, the effectiveness of the background echo and backscattered signal computational classification, and to detect and characterize the microstructure changes, i.e., the formation of the secondary phases/precipitates, occurring in a thermally aged Inconel 625 alloy at 650 °C for 10, 100 and 200 h. To accomplish these goals, background echo and backscattered signals pre-processed by the detrended-fluctuation and rescaled range methods and without any pre-processing were used. The classification of the pre-processed and original signals was carried out using the Karhunen–Loève Transform. The potentiality and efficiency of the combination of the ultrasonic signals and the computational tools to characterize the microstructures of Inconel 625 alloy samples aged and as-welded was demonstrated by the results.

As far as the authors know, this is the first time that the effect of thermal aging on Inconel 625 alloy has been analyzed using two types of ultrasonic signals combined with computational tools of signal pre-processing and classification, which makes the results presented and discussed of noteworthy value.

2. Experimental procedures

This section described the experimental work done; first; the test setup is described; then, the preparation of the Inconel 625 alloy samples is addressed; afterwards, the ultrasonic inspection is introduced; finally, the methods and techniques used to process and classify the ultrasonic signals are presented.

2.1. Test setup

Inconel 625 alloy coatings deposited on an ASTM A36 steel metal base were used in the experiments. The chemical compositions of these materials are shown in Table 1. A 4 mm diameter tungsten electrode doped with thorium was used, and pure argon (99.99%) was chosen as the shielding gas.

An electronic multi-process power source connected to the data acquisition system was used during the welding to monitor the current and tension. The manipulation of the torch was carried out using an industrial robot system, Fig. 1a. An automatic cold wire feed system for gas tungsten arc welding (GTAW) was used to supply the filler metal. A positioning unit was used to guide the wire into the arc so that adjustments to the configuration parameters and geometry of the wire feed could be made,

Table 1
Chemical composition in weight percent (wt.%) of the weld metal/coating and of the base metal.

AWS ERNiCrMo-3 (INCONEL 625 alloy – Weld Metal)	**Ni**	**C**	**Cr**	**Mo**	**W**	**Fe**	**Al**	**Ti**
	64.43	0.011	22.2	9.13	–	0.19	0.09	0.23
	Nb	**Mn**	**Si**	**Cu**	**Co**	**V**	**P**	**S**
	3.53	0.01	0.05	0.01	0.03	–	0.002	0.002
ASTM A36 steel (Base Metal)	**Ni**		**C**		**Cr**		**Mo**	
	0.02		0.23		0.02		–	
	Fe		**Al**		**Mn**		**Si**	
	Bal.		0.03		0.67		0.09	

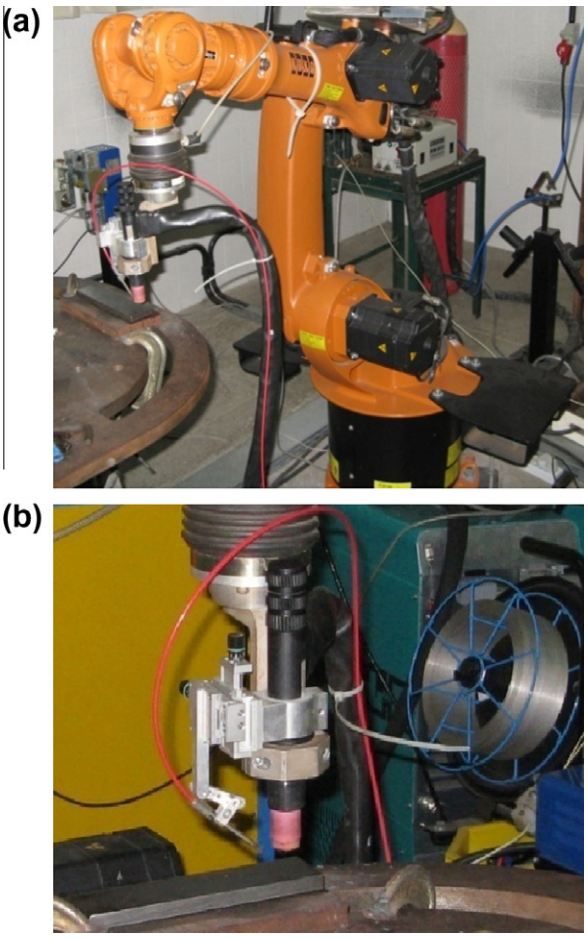

Fig. 1. Experimental setup used in the welding process: (a) robotic system, (b) GTAW guide wire feed and torch.

Fig. 1b. The welding coating was performed on an ASTM A36 steel metal base plate, resulting in a coating of $350 \times 60 \times 14\ mm^3$. The remaining welding parameters used were: 285 A of welding current (DCEN), arc voltage of 20 V, travel speed equal to 21 cm/min, welding heat input of 16 kJ/cm, wire feed speed equal to 6.0 m/min, arc length of 10 mm, 15 l/min of gas flow and arc oscillation describing a double-8 trajectory. Other minor considerations included the wire feed direction ahead of the arc weld, wire tip to pool surface was kept at a distance of 3 mm, wire feeding angle was maintained constant and equal to 50°, Fig. 3, and the electrode tip angle fixed at 50°. To guarantee a good overlaying due to multiple pass deposited side by side, a distance equal to 2/3 of the initial weld bead width was established as an ideal step. Other arc oscillating parameters were: oscillation amplitude of 8 mm and wave length equal to 1.2 mm.

To produce a 10 mm thick coating on the substrate, seven layers with eight passes were deposited under identical welding conditions.

2.2. Samples preparation

After the welding, the coating was detached from the substrate by conventional machining, as the material of interest was only the Inconel 625 alloy. Then, the coating was divided into four samples, three samples were submitted to aging heat treatments at 650 °C for times of 10, 100 and 200 h [24], and the remaining one was kept as the as-weld state (0 h). The aged samples were water cooled with moderate agitation at room temperature.

Afterwards, the four samples were subjected to metallographic preparation that included grinding, polishing and electrolytic etching using 10% chromic acid with a tension of 2 V tension for 15 s. Metallographic images were acquired using a scanning electron microscope (SEM) Philips XL30 (Oxford Instruments, England), and a study of the chemical composition of the secondary phases was carried out through energy dispersive spectroscopy of X-rays (EDS).

After the microstructural analysis, nondestructive ultrasonic inspection was conducted to attain velocity and attenuation measurements, as well as the acquisition of background echo and backscattered signals to evaluate the effect of aging on the Inconel 625 alloy samples.

2.3. Ultrasonic inspection

For the ultrasonic inspection, the pulse echo technique and direct contact method were used to obtain ultrasonic velocity and attenuation measurements. As a coupling material, SAE 15W40 lube oil was used for the longitudinal measurements. A Krautkramer ultrasound device (GE Inspection Technologies, USA, model USD15B) was used connected to a 100 MHz digital oscilloscope (Tektronix, USA, model TDS3012B), which transmits the ultrasonic signals to a computer, so they can be processed. Ten signals were acquired with 10,000 points and a sampling rate of 1 Gs/s, after which the average ultrasound velocity and attenuation values were calculated.

The ultrasonic velocity measurements of all the samples were obtained by using commercial NDT ultrasonic transducers: one of 4 MHz (Krautkramer, Germain, model MB4S) and another one of 5 MHz (Krautkramer, Germain, model MSW-QCG). The choice of these transducers was based on the authors' previous experience in this kind of NDT and knowledge concerning the materials under study [21–23]. In fact, these frequencies revealed to be the most adequate to analyze the material under study, as a transducer with a frequency of 10 MHz completely attenuated the ultrasound signal, and one with a frequency of 2.25 MHz led to an adjacent echo that overlapped extensively the signal compromising seriously the accuracy of the results.

For each sample, 10 signals with two adjacent echoes per signal were acquired for the velocity measurements. Next, the time between the first two echoes was measured through an echo overlapping algorithm [23]. With the wave propagation time and the thicknesses of the samples, obtained by using a micrometer at the same signal acquisition points, it was possible to determine the average velocity of wave propagation and the ultrasonic attenuation coefficient [23,25].

2.4. Ultrasonic signal processing and classification

Classification of the ultrasound signals was carried out using the Karhunen–Loève Transform and pre-processing techniques based on detrended fluctuation analysis (DFA), statistical and Hurst RS methods, as well as background echo and backscattered signals without any pre-processing. To assurance statistical significance in the measurement processes, 40 signals were acquired for each sample, each background echo signal had 10,000 points, i.e. a total of 400,000 points was attained, and each backscattered signal had 500 points, resulting in a total of 20,000 points to study. After signal pre-processing using the DFA and RS methods, the number of points of the background echo signals was reduced to 1680, i.e. a reduction of 42 times, and to 960 points for the backscattered signals, which means a reduction of 24 times. As the echo signals without pre-processing had a very large number of points, their use was impracticable.

2.4.1. Fluctuation analyze

This section describes the methods of fluctuation analyze used in the signal pre-processing step for the classification of the alloy microstructures. These methods are usually employed to identify long-term memory effects in self-affine or fractal time series [26–28]. In a time series of a genuine fractal nature, memory effects can be gauged by a single number, η, that relates to a measure of the average fluctuations, $Q(\tau)$, inside the time series to the size, τ, of the time window used in the calculation, according to the power law:

$$Q(\tau) \sim \tau^{\eta}. \tag{1}$$

For experimental time series, which of course cannot be genuinely fractal, the various analyses described below have proven to be quite useful in providing signatures of the underlying processes peculiar to distinct situations, such as different defects present in welding joints probed by ultrasonic techniques [26], as well as diverse defects in gearboxes registered by vibration signals [27].

Each technique involves the calculation of the average of the functions $Q(\tau)$ over all cells, for a defined set of values of τ, which are then used to characterize the different microstructures, since the exponents η are not sufficient to generate the desired discrimination.

2.4.1.1. Rescaled-range method. The rescaled-range (RS) method was introduced by Hurst [28] as a tool for evaluating the persistence or anti-persistence of a time series. The method works by dividing the series into intervals of a given size τ, and calculating the average ratio RS of the range, i.e., the difference between the maximum and minimum values of the series, to the standard deviation inside each interval. The size τ is then varied, and a curve of the rescaled range RS as a function of τ is obtained [28].

2.4.1.2. Detrended-fluctuation analysis. The detrended-fluctuation analysis (DFA) aims at improving the evaluation of correlations in a time series by eliminating trends in the data. The method consists initially in obtaining a new integrated series:

$$\tilde{z}_i = \sum_{k=1}^{i} (z_k - \langle z \rangle), \tag{2}$$

with the average $\langle z \rangle$ being taken over all n points [29].

After dividing the series into L, with $L = \mathrm{int}[n/\tau]$, intervals of size τ, the points inside a given interval are fitted by a straight line. Then, for eliminating linear trends, a detrended-variation function $\Delta_i(\tau)$, for each interval, τ is obtained by subtracting from the integrated date the local trend as given by the linear fit. The detrended-variation function is explicitly defined as:

$$\Delta_i(\tau) = \tilde{z}_i - h_i(\tau), \tag{3}$$

where $h_i(\tau)$ is the value associated with point i according to the linear fit [29]. Finally, the root-mean-square fluctuation $F(\tau)$ inside an interval can be calculated as, [29]:

$$F(\tau) = \sqrt{\frac{1}{\tau} \sum_i \Delta_i^2(\tau)}. \tag{4}$$

2.4.2. Karhunen–Loève transformation

In order to classify the signal data pre-processed by applying the statistical fluctuation (DFA) and rescaled-range (RS) methods on the ultrasonic signals acquired, the Karhunen–Loève transformation was used.

Although very helpful in studying data clusters, any computational approach ignores some of the information embraced in the original data. For example, the original Karhunen–Loève (KL) transformation does take into account all class information in the classification process. The version of KL transformation employed here [30] relies on the compression of discriminatory information contained in the class means.

Let $\mathbf{x}_i$ be the vector corresponding to the input signal. KL transformation consists of initially projecting the training vectors along the eigenvectors of the within-class covariance matrix $\mathbf{S}_W$, defined by:

$$\mathbf{S}_W = \frac{1}{N} \sum_{k=1}^{N_C} \sum_{i=1}^{N_k} y_{ik} (\mathbf{x}_i - \mathbf{m}_k)(\mathbf{x}_i - \mathbf{m}_k)^{\mathbf{T}}, \tag{5}$$

where N_C is the number of different classes, N_k is the number of vectors in class k, $\mathbf{m}_k$ is the average vector of class k, and T denotes the transpose of a matrix (here, a column vector). The element y_{ik} is equal to 1 (one), if $\mathbf{x}_i$ belongs to class k, otherwise y_{ik} equals 0 (zero). The resulting vectors are rescaled by a diagonal matrix built from the eigenvalues λ_j of $\mathbf{S}_W$. In the matrix notation, this operation can be written as:

$$\mathbf{X}' = \Lambda^{-\frac{1}{2}} \mathbf{U}^T \mathbf{X}, \tag{6}$$

where $\mathbf{X}$ is the matrix whose columns are the training vectors $\mathbf{x}_i$, $\Lambda = diag(\lambda_1, \lambda_2, \ldots)$, and $\mathbf{U}$ is the matrix whose columns are the eigenvectors of $\mathbf{S}_W$. This choice of coordinates assures that the transformed within-class covariance matrix corresponds to the unit matrix. Finally, in order to compress the class information, the resulting vectors are projected onto the eigenvectors of the between-class covariance matrix $\mathbf{S}_B$:

$$\mathbf{S}_B = \sum_{k=1}^{N_C} \frac{N_k}{N} (\mathbf{m}_k - \mathbf{m})(\mathbf{m}_k - \mathbf{m})^{\mathrm{T}}, \tag{7}$$

where $\mathbf{m}$ is the overall average vector. The full transformation can be written as:

$$\mathbf{X}'' = \mathbf{V}^T \Lambda^{-\frac{1}{2}} \mathbf{U}^T \mathbf{X}, \tag{8}$$

with $\mathbf{V}$ as the matrix whose columns are the eigenvectors of $\mathbf{S}_B$ (calculated from (6)) [30].

3. Experimental results and discussion

In this section, the experimental results are discussed: first, the SEM and EDS analyses of the Inconel 625 alloy aged samples are discussed; then, the ultrasound velocity and attenuation values are evaluated; and, finally, the classification of the ultrasound signal classification and their correlation with the material microstructures are discussed.

3.1. SEM/EDS analysis

The coatings of Inconel 625 alloy deposited by the welding process were submitted to metallographic analysis and SEM revealed the Ni-fcc matrix and an extensive amount of secondary phases precipitated (glowing dots) at the intercellular or interdendritic region. The microstructure of the as-welded alloy condition (0 h) can be seen in Fig. 2a. Figs. 2b–d show the micrographs of the aged samples at 650 °C for 10, 100 and 200 h, respectively, in which the microstructural modifications can be seen clearly.

A detailed investigation of all samples was carried out by SEM/EDS. Fig. 3a shows the microstructure of the as-welded condition. An enlarged area of this image depicting an interdendritic secondary phase and some precipitates with cuboidal morphology is shown in Fig. 3b. EDS analysis of the same area, shows an intense peak of Nb, corresponding to an expressive increase of this element in the secondary phase, Fig. 3c. The Nb content was four times higher than the normal content for the alloy, revealing that an Nb rich Laves phase was formed after welding. A cuboidal morphology

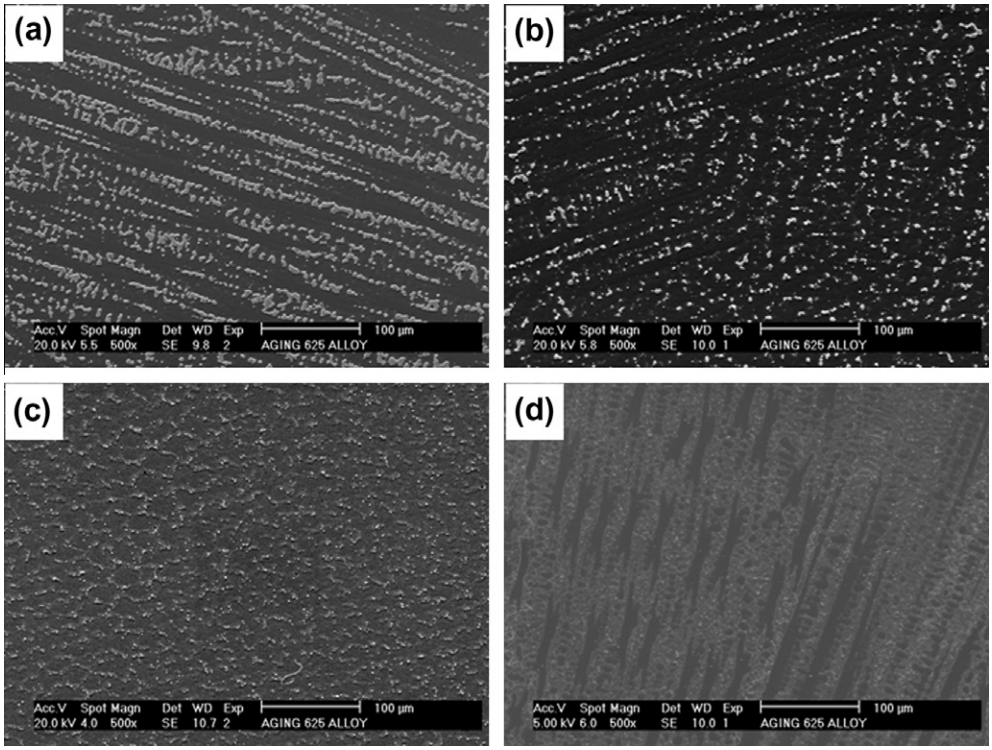

Fig. 2. SEM micrographs using secondary electrons showing the Ni-fcc matrix and the secondary phases: As-welded (a), and aged at 650 °C for 10 (b), 100 (c) and 200 (d) h.

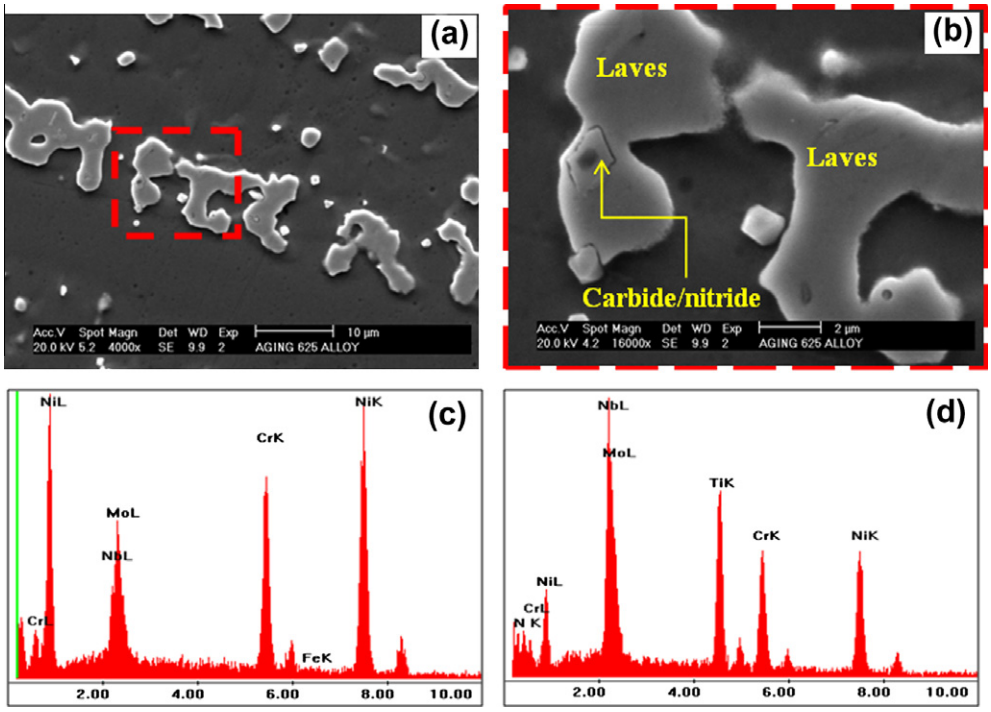

Fig. 3. Representative microstructure of the sample in as-welded condition (a), detail view showing large blocks of Laves phases with some cuboidal precipitates of carbides/nitrides (b), EDS analysis of Laves phase rich in Nb (c), and of a cuboidal precipitate rich in Ti and Nb (d).

particle enclosed inside the Laves phase was evaluated by EDS and the result showed an intense peak of Nb and also the presence of a strong peak of Ti, besides the presence of the Nb peak, as can be seen in Fig. 3d. Based on these findings, one can affirm that a cuboidal precipitation took place forming Nb and Ti nitrides and/or carbonitride elements. In the work of Silva et al. [31] microstructures of an Inconel 625 alloy weld overlay were investigated by transmission electron microscopy and cuboidal precipitates rich in Nb and Ti present in the weld metal were identified not as carbonitrides (NbTi)(CN), but as a combination of a titanium

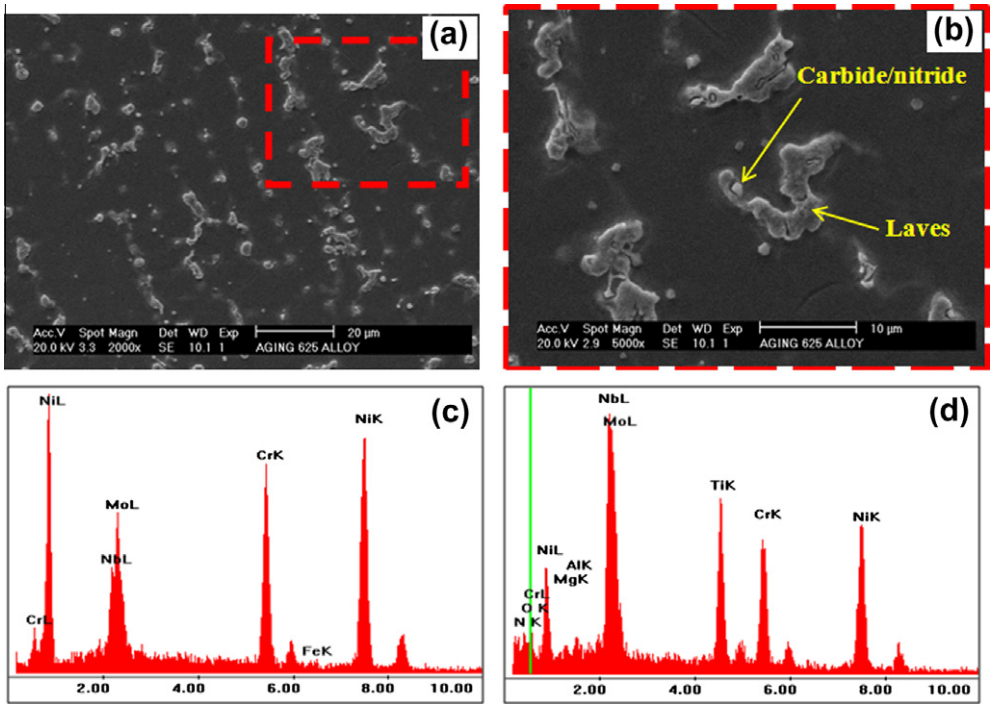

Fig. 4. Representative microstructure of the sample aged at 650 °C for 10 h (a), detail view showing Eutectic-like Laves phase and some cuboidal precipitates of carbides/nitrides (b), EDS analysis of Laves phase rich in Nb (c), and of a cuboidal precipitate rich in Ti and Nb and showing also N, O, Mg and Al (d).

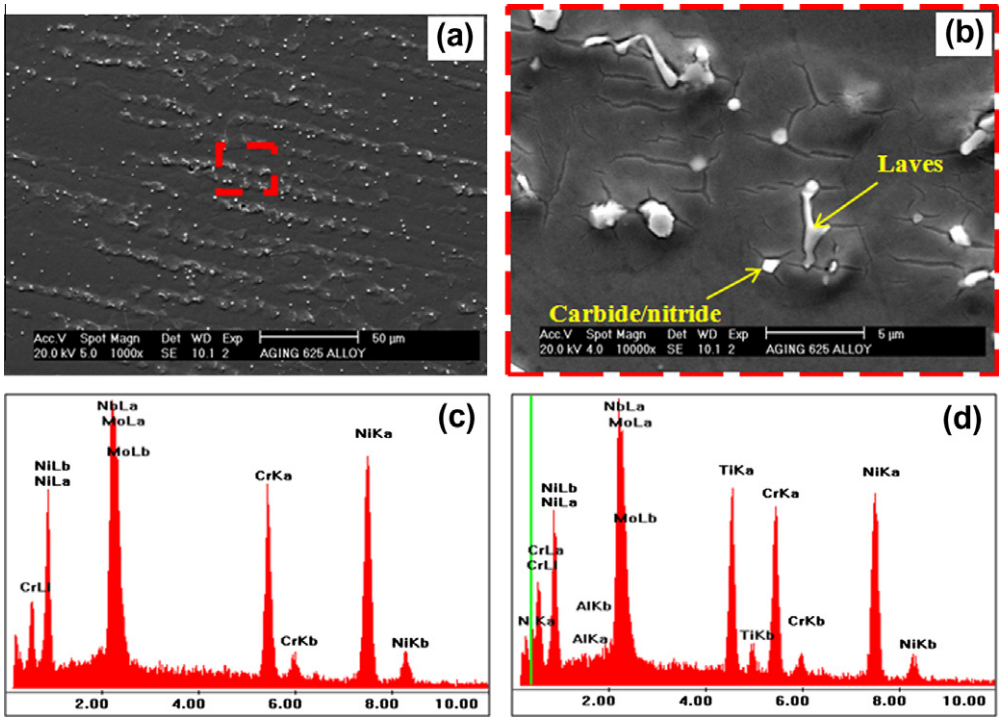

Fig. 5. Representative microstructure of the sample aged at 650 °C for 100 h (a), detail view showing decomposition of the Laves phase reducing significantly its dimension with some cuboidal precipitates of carbides/nitrides (b), EDS analysis of Laves phase rich in Nb (c), and of a cuboidal precipitate rich in Ti and Nb (d).

nitride (TiN) core surrounded by a shell composed of niobium and/or niobium–titanium carbide (NbTi)C. This hypothesis was supported by the heterogeneous chemical composition observed by EDS elemental mapping, which showed a new combination of a titanium nitride (TiN) core surrounded by a shell composed of niobium (NbC) and/or niobium–titanium (NbTi)C carbides [32].

Fig. 4a shows the microstructure correspondent to the sample aged at 650 °C for 10 hours. Additionally, Fig. 4b shows a detail of the microstructure in which one can see the presence of Laves phase and some cuboidal precipitates of carbides/nitrides. The EDS analysis of the Laves phase rich in Nb and cuboidal precipitates rich in Ti and Nb, and also revealing N, O, Mg and Al, are

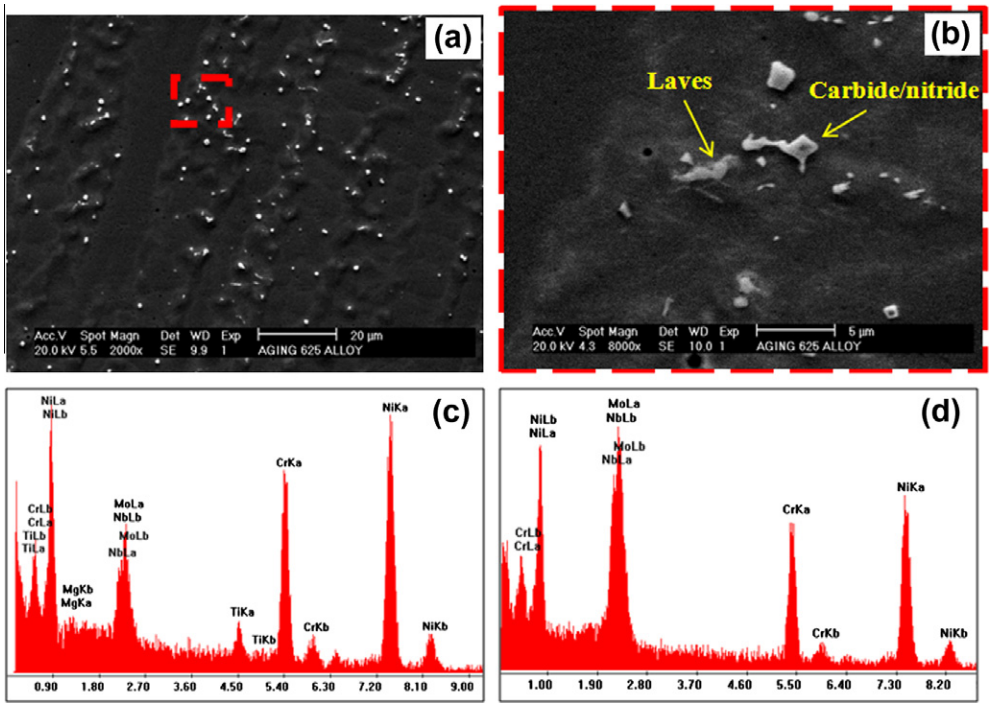

Fig. 6. Representative microstructure of the sample aged at 650 °C for 200 h showing practically only TiNb carbides/nitrides (a), a detailed view showing a reminiscent of the Laves phase indicating almost total dissolution/decomposition of the same (b), EDS analysis of Laves phase rich in Nb (c), and of a cuboidal precipitate rich in Ti and Nb (d).

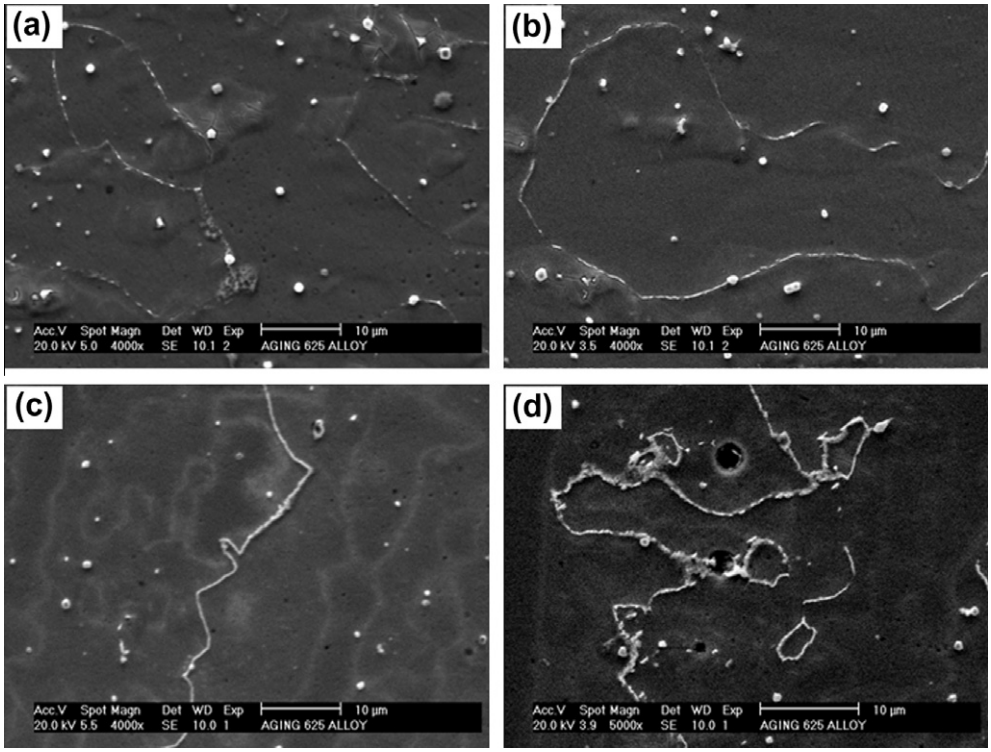

Fig. 7. Grain boundary precipitation in an early stage observed in the sample aged at 650 °C for 100 h (a and b), and in the final stage observed in the sample aged at 650 °C for 200 h (c and d).

shown in Fig. 4c and d. The findings confirmed a large amount of Laves phase, but signs of Laves phase dissolution were also noted.

Increasing the time of thermal exposure to 100 h, a significant change in the alloy microstructure relative to the as-weld and 10 h conditions was observed. There was a considerable reduction in Laves phase content and dimension, Fig. 5a. The resulting microstructure showed a very reduced amount of Laves phase due to the partial dissolution of the same, Fig. 5b. The carbide/nitrides that remained seemed to be unaffected, without any sign of dissolution. So, quantitatively there was a larger amount of TiNb cabides

Table 2
Ultrasound velocity values.

Temperature	Transducer frequency (MHz)	Aging time (h)	Velocity (m/s)								Mean (m/s)	Standard deviation
0 h (as-welded)	4	–	5822	5840	5834	5866	5900	5905	5873	5900	5868	33
	5	–	5826	5793	5820	5856	5923	5889	5923	5890	5865	49
650 °C	4	10	5899	5855	5844	5833	5854	5702	5789	5837	5827	59
		100	5748	5768	5760	5711	5725	5715	5721	5682	5729	28
		200	5863	5923	5923	5838	5793	5758	5841	5800	5842	60
	5	10	5914	5858	5827	5823	5798	5730	5782	5817	5819	54
		100	5724	5721	5760	5740	5732	5678	5711	5682	5719	28
		200	5896	5821	5837	5812	5819	5746	5828	5789	5819	42

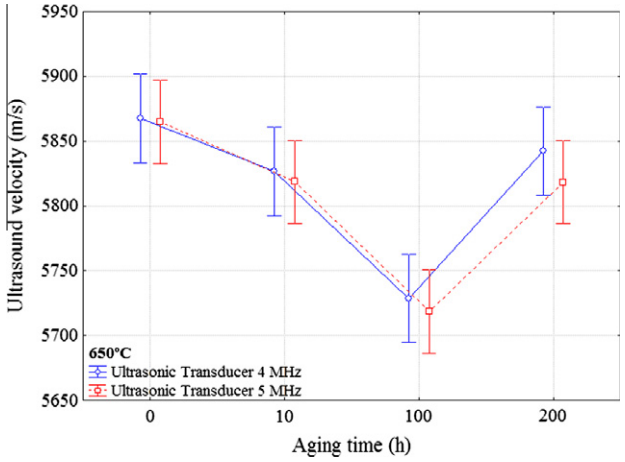

Fig. 8. Ultrasound velocities for *each thermal* aging time at 650 °C.

/nitrides relative to the Laves phases, which was different to what was seen in the as-welded and 10 h samples.

A representative microstructure of the Inconel 625 alloy sample aged at 650 °C for 200 h is shown in Fig. 6a. In this case, the microstructure indicated an almost complete dissolution of the Laves phases, as the microstructure was now practically totally constituted by TiNb carbides/nitrides and Ni-fcc matrix. The yet incomplete Laves phase dissolution was evidenced by the residual presence of reminiscent Laves phase, as shown in Fig. 6b. The EDS analysis of Laves phase rich in Nb and some cuboidal precipitate rich in Ti and Nb are shown in Fig. 6c and d.

Another important microstructural change that was observed in samples aged for 100 and 200 h was the precipitation of new particles in the solidification grain boundaries and solidification sub-grain boundaries, as depicted in Fig. 7. Figs. 7a and b illustrate the behavior of the precipitation for the 100 h aging condition, in which a discontinuous precipitation of very thin precipitates along the grain boundaries is seen. For the 200 h aging a continuous thin film precipitate along the grain boundaries was observed in most cases, as shown in Fig. 7c. In the remaining cases, discontinuous films were formed, but there were more precipitates than for 100 h of aging, Fig. 7d.

3.2. Ultrasound velocity and attenuation

The ultrasound velocities obtained using the transducers with frequencies of 4 and 5 MHz from the as-welded and aged at temperatures of 650 °C for 10, 100 and 200 h samples are shown in Table 2 and represented in Fig. 8.

From Fig. 8, one can see that the mean ultrasound velocity decreased with the time of the aging heat treatment between 0 h (as-welded) and 100 h, and increased from 100 to 200 h. This behavior was found for all frequencies used, indicating the presence of two stages: (i) dissolution of the Laves phases for 0–100 h and (ii) appearance of cuboidal precipitates rich in Ti and Nb from 100 to 200 h.

Based on Kumar et al. [33], who studied a service tube of Inconel 625 alloy exposed to ~600 °C for ~60,000 h, a short duration aging at 650 °C up to 10 h caused a dissolution of the Ni_2(Cr,-Mo) phase. When the alloy was aged at 850 °C for 1 h, there was a complete dissolution of both γ'' and Ni_2(Cr,Mo) precipitates. It is important to note that this temperature is 200 °C higher than the one used in this work. Other temperature ranges were studied by Kumar et al. [33], for example, 1150 °C for 0.5 h, in which a full dissolution of the intermetallic precipitates and grain boundary carbides occurred. Aging the alloy led to the precipitation of γ'' phase at 650 °C and δ phase at 850 °C. Details on the microstructural characterization of the Inconel 625 alloy aged and analyzed by Kumar et al., in which the precipitates were evaluated by optical microscope and transmission electron microscope, were reported by Shankar et al. [24]. These works support the values of ultrasound velocities obtained in this study at 650 °C, Fig. 8; in particularly, the higher value for the as-welded material, due to the presence of the intermetallic phases, and a lower value for aging at 10 h. The lowest velocity value was found in the sample aged for 100 h, indicating the dissolution of precipitates after welding, i.e. the formation of the secondary phases. According to Kumar et al. [33], the dissolved precipitates are only of the Ni_2(Cr, Mo) type. The maximum reduction in the ultrasonic velocity was observed after 200 h of aging. Probably, at this aging time, the initial formation of a new phase, or morphology changes and/or variation in the amount of the secondary phases, occurred. The results reported through to 200 h of aging were confirmed in this work, since there was a dissolution/decomposition of the Laves phases over the aging time.

The ultrasonic velocity is affected by the density and the elastic constants of the material under inspection [34,35] and, mainly, by its different micro, including grain size and shape, precipitations/new phases, distortions in the crystallographic lattice, pores and several types of discontinuity [36–38]. However, the degree of coherency, fineness or distribution of the precipitates cannot originate variations in ultrasonic velocity [33]. Therefore, the variations observed in the ultrasound velocity indicate changes in the material properties due to secondary phases generated by the weld solidification process.

In order to measure the intrinsic attenuation of the material, the ultrasonic testing must be performed with care, as many factors can contribute to its inaccuracy, such as beam divergence (i.e. diffraction) [39], coupling materials in the direct contact technique, unsteady pressure applied to the transducer and roughness [40]. These factors mentioned above can cause difficulties to correlation the ultrasound attenuation with microstructure, as was observed by Bouda et al. [41,42]. However, in our work the ultrasound attenuation values were similar to the ones obtained through ultrasound velocity until 100 h for the temperature used, as can be

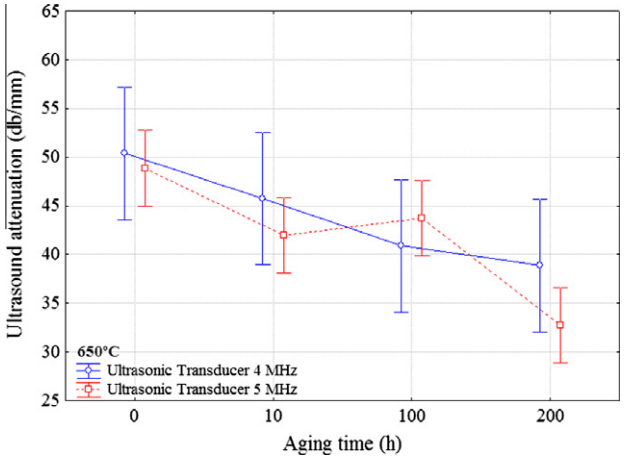

Fig. 9. Ultrasound attenuations for *each thermal* aging time at 650 °C.

seen in Fig. 9. This figure, which is built from the values in Table 3, shows that at 200 h the reverse of what occurred for the ultrasound velocity occurred, i.e., the ultrasound attenuation value continues to decrease due to the dissolution of the Laves phases and there is a considerable formation of cuboidal precipitates rich in Ti and Nb. This reveals that the ultrasonic velocity and attenuation are promising indicators for following-up the phase transformations of the material, since that are affected by the intermetallic precipitates and probably by the grain boundary carbides in the Inconel 625 alloy studied in this work.

3.3. Ultrasound signal classification and microstructural correlation

The results using the original ultrasound background echo and backscattered signals and the correspondent pre-processed signals, both classified using Karhunen–Loève Transform, proved to be efficient in the recognition and classification of the secondary phases originated by the thermal aging process. The analysis of the classification results was accomplished using confusion matrices, also known as confusion tables [43]. One hundred training sets were used to build all the confusion matrices and the diagonals of such matrices indicate the average accuracy rate values. Table 4 shows the confusion matrix for the four classes classified (0 h (as-welded) and 10, 100 and 200 h at 650 °C). The values in this table were obtained using the 5 MHz transducer, backscattered signals and with RS signal pre-processing. From these values, a correct classification of 55% for 0 h, and of 40%, 53% and 96% for 10, 100 and 200 h, can be confirmed respectively. There was greater difficulty in the classification for 0, 10 and 100 h at 650 °C than the classification for 200 h at the same temperature. These findings are fully supported by the microstructural analysis that was carried out, since the time period between 0 and 100 h corresponded to the formation and partial dissolution of the Laves phases, and the time period from 100 h to 200 h corresponded to the cuboidal precipitation rich in Ti and Nb, i.e., two microstructure types were involved. The average classification accuracy rate was equal to 61% and required a computational time of 79.1250 s in a personal computer with an Intel Pentium D915 Duo Core at 2.8 GHZ and 1 G of RAM.

Table 4
Confusion values for conditions: 0 h (as-welded) and 10, 100 and 200 h at 650 °C, using backscattered signal, RS pre-processing and a 5 MHz transducer.

	0 h (%)	10 h – 650 °C (%)	100 h – 650 °C (%)	200 h – 650 °C (%)
Classified as 0 h	55	24	14	4
Classified as 650 °C (10 h)	20	40	32	0
Classified as 650 °C (100 h)	24	33	53	0
Classified as 650 °C (200 h)	1	3	1	96

Table 5
Confusion values for conditions: 0 h (as-welded) and 10, 100 and 200 h at 650 °C, using backscattered signal, without signal pre-processing and a 4 MHz transducer.

	0 h (%)	10 h – 650 °C (%)	100 h – 650 °C (%)	200 h – 650 °C (%)
Classified as 0 h	72	7	1	0
Classified as 650 °C – 10 h	23	78	15	0
Classified as 650 °C – 100 h	5	15	84	0
Classified as 650 °C – 200 h	0	0	0	100

However, when backscattered signals without pre-processing and a 4 MHz transducer were used, a substantial increase in the accuracy rate was observed. Table 5 shows a correct classification of 72% for 0 h, and of 78%, 84% and 100% for 10, 100 and 200 h at 650 °C, respectively. In this case, the average classification accuracy rate was equal to 83.50% and required a computational time of 811.6560 s. Again, there was a greater difficulty to classify the signals acquired for aging times of 0, 10 and 100 h, but the ones acquired for the aging time of 200 h were accurately classified. In comparison to the classification approach based on signal pre-processing, the classification rate increased by 22.5%; however, the required computational time was considerably greater, as can be seen in Table 6. As such, it is possible to confirm the efficiency of the ultrasonic nondestructive inspection technique combined with the computational signal pre-processing and classification tools used to monitor the formation of new phases of the Inconel 625 alloy originated by thermal aging.

The results obtained for all testing conditions are shown in Table 6, which demonstrates the accuracy rate and the required classification time. The experimental findings show that a superior accuracy was reached with the 4 MHz transducer and original backscattered signals, i.e. without any pre-processing, although a greater classification time was required due to the larger amount of data involved. For this reason, many researchers have used signal pre-processing techniques to optimize the required computational

Table 3
Ultrasound attenuation values.

Temperature	Transducer frequency (MHz)	Aging time (h)	Attenuation (db/mm)								Mean (m/s)	Standard deviation
0 h (as-welded)	4	–	73	65	48	36	47	43	51	40	50	13
	5	–	48	54	52	45	49	39	51	53	49	5
650 °C	4	10	42	44	32	59	28	49	57	55	46	11
		100	38	29	41	41	47	47	37	47	41	6
		200	38	36	49	43	39	36	35	35	39	5
	5	10	53	48	47	35	36	38	32	47	42	8
		100	47	37	45	42	51	41	46	41	44	4
		200	38	35	36	29	31	29	29	35	33	4

Table 6
Results obtained for all experimental conditions.

Transducer frequency (MHz)	Type of signal	Pre-processing technique	0 h (as-welded), and 10, 100 and 200 h at 650 °C	
			Accuracy rate (%)	Classification time (s)
4	Backscattered	DFA	56.25	78.84
		RS	42.25	78.64
		–	83.50	811.66
	Background echo	DFA	49.50	237.58
		RS	45.50	234.34
5	Backscattered	DFA	75.00	78.72
		RS	61.00	79.13
		–	67.75	856.25
	Background echo	DFA	59.25	232.38
		RS	38.50	236.97

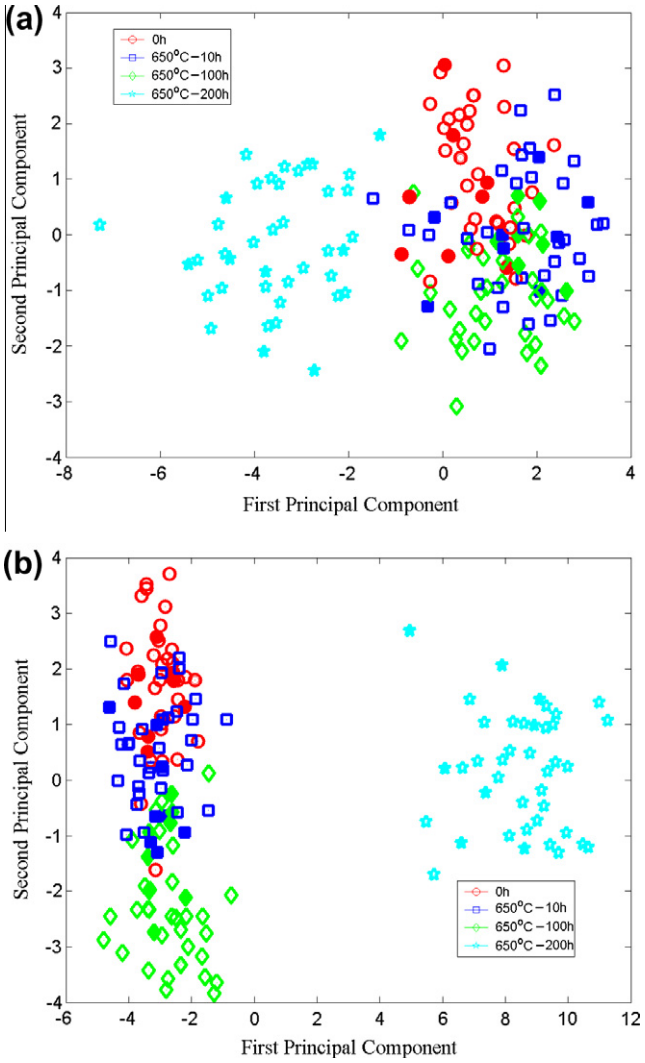

Fig. 10. Classification obtained from the backscattered signals, using RS signal pre-processing and a 5 MHz transducer for aging times of: 0 h and 10, 100 and 200 h at 650 °C (a), and from the same signals and aging times but without signal pre-processing and using a 4 MHz transducer (b).

time. In this work, the best classification rate (83.5%) was attained using a 4 MHz transducer and the original backscattered signals.

The best combination accomplished based on signal pre-processing techniques was using a 5 MHz transducer, backscattered signals and DFA. In fact, the DFA signal pre-processing presented more accurate results than the RS method, and the backscattered signals were more favorable than the background echo signals.

Figs. 10a and b illustrate a combination of the data in Tables 4 and 5, respectively, making the graphical analysis of the signal classifications possible. As such, in these images one can recognize patterns and discriminate differences among the distinct types of ultrasound signals and thermal aging conditions.

4. Conclusions

This work evaluated the sensitivity of the ultrasound velocity and attenuation, and original and pre-processed background echo and backscattered signals for a fast, accurate and nondestructive analysis of the secondary *phase formation* of a welded and aged Inconel 625 alloy.

For the work done, the following conclusions can be pointed out:

(1) The results revealed that the ultrasonic measurements were sensitive to the microstructural changes in the Inconel 625 alloy, and were able to identify the formation of the secondary phases during the welding process, as well as the modifications due to the different thermal aging times.
(2) The maximum ultrasound velocity was obtained in the as-welded material, in which the secondary phases of intermetallic precipitates were formed. Until 100 h, there was a decrease in the ultrasound velocity due to the dissolution of precipitates. For 200 h, the velocity increased due to the formation of new phases and there was a large reduction/decomposition of the Laves phases. An important observation was that the ultrasound velocity was influenced by the intermetallic precipitates and formation of the cuboidal precipitate rich in Ti and Nb.
(3) In relation to the ultrasound signal classification, the best accuracy (around 83.5%) was obtained using the 4 MHz transducer and with the original signals, i.e. without signal pre-processing. Regarding the signal pre-processing, the DFA method presented more accurate results than the RS method, the same was seen with the backscattered signals in relation to background echo signals.

In general, the outcomes obtained and discussed throughout this work are very promising and can significantly contribute to the field of Materials Science and Engineering, since the nondestructive characterization of materials and microstructural control based on ultrasonic measurements combined with computational techniques can lead to more effective results for the mechanical characterization of materials, in particular, of the Inconel 625 alloy.

Acknowledgments

The first author thanks the National Council for Research and Development (CNPq) and the Cearense Foundation for the Support of Scientific and Technological Development (FUNCAP) for providing financial support for a DCR grant (Project number 35.0053/2011.1) from UNIFOR, in Brazil.

All authors are also grateful for the support given by the following laboratories of the Federal University of Ceará: Welding Engineering Laboratory (ENGESOLDA), Materials Characterization Laboratory (LACAM), Center of Non-Destructive Testing (CENDE), as well as for the financial support given by the Research and Projects Financing (FINEP), Coordination for the Improvement of People with Higher Education (CAPES) and finally to Petróleo Brasileiro S.A (Petrobras).

References

[1] Mathew MD, Rao KBS, Mannan SL. Evaluation of Mechanical Properties of Aged Alloy 625 Nickel Base Superalloy using Nondestructive Ball Indentation Technique. In: Kim SY editor. Proceedings of 15th international conference on structural mechanics in reactor technology (SMiRT-15), Seoul, Korea, 1999.

[2] Thomas C, Tait P. The performance of Alloy 625 in long-term intermediate temperature applications. Int J Press Vessel Piping 1994;59:41–9.

[3] Kohla HK, Peng K. Thermal stability of the superalloys Inconel 625 and Nimonic 86. J Nucl Mater 1981;101:243–50.

[4] Boser O. The behavior of Inconel 625 in a silver environment. Mater Sci Eng 1979;41:59–64.

[5] Cieslak MJ, Headley TJ, Romig AD. The welding metallurgy of HASTELLOY alloys C-4, C-22 and C-276. Metall Mater Trans A 1986;17A(1986):2035–47.

[6] Cieslak MJ. The welding and solidification metallurgy of alloy 625. Weld J 1981;70:49–56.

[7] Yang JX, Zheng Q, Sun XF, Guan HR, Hu ZQ. Formation of μ phase during thermal exposure and its effect on the properties of K465 superalloy. Scripta Mater 2006;55:331–4.

[8] Dupont JN, Banovic SW, Marder AR. Microstructural evolution and weldability of dissimilar welds between a super austenitic stainless steel and nickel-based alloys. Weld R 2003;82:125–56.

[9] Evans ND, Maziasz PJ, Shingledecker JP, Yamamoto Y. Microstructure evolution of alloy 625 foil and sheet during creep at 750 °C. Mater Sci Eng A 2008;498:412–20.

[10] Mathew MD, Murty KL, Rao KBS, Mannan SL. Ball indentation studies on the effect of aging on mechanical behavior of alloy 625. Mater Sci Eng A 1999;264:159–66.

[11] Zhang D, Harris SJ, McCartney DG. Microstructure formation and corrosion behaviour in HVOF-sprayed Inconel 625 coatings. Mater Sci Eng A 2003;344:45–56.

[12] Ganesh P, Kaul R, Paul CP, Tiwari P, Rai SK, Prasad RC, et al. Fatigue and fracture toughness characteristics of laser rapid manufactured Inconel 625 structures. Mater Sci Eng A 2010;527:7490–7.

[13] Cooper KP, Slebodnick P, Thomas ED. Seawater corrosion behavior of laser surface modified Inconel 625 alloy. Mater Sci Eng A 1996;206:138–49.

[14] Arafin MA, Medraj M, Turner DP, Bocher P. Transient liquid phase bonding of Inconel 718 and Inconel 625 with BNi-2: modeling and experimental investigations. Mater Sci Eng A 2007;447:125–33.

[15] Mathew MD, Rao KBS, Mannan SL. Creep properties of service-exposed Alloy 625 after re-solution annealing treatment. Mater Sci Eng A 2004;372:327–33.

[16] Song KH, Nakata K. Effect of precipitation on post-heat-treated Inconel 625alloy after friction stir welding. Mater Des 2010;31:2942–7.

[17] Li D, Guo Q, Guo S, Peng H, Wu Z. The microstructure evolution and nucleation mechanisms of dynamic recrystallization in hot-deformed Inconel 625superalloy. Mater Des 2011;32:696–705.

[18] Ezugwu EO, Wang ZM, Machado AR. The machinability of nickel-based alloys: a review. J Mater Process Technol 1998;86:1–16.

[19] Kumar A, Rajkumar KV, Jayakumar T, Raj B, Mishra B. Ultrasonic measurements for in-service assessment of wrought Inconel 625 cracker tubes of heavy water plants. J Nucl Mater 2006;350:284–92.

[20] Palanichamy P, Mathew MD, Latha S, Jayakumar T, Rao KBS, Mannan SL, et al. Assessing microstructural changes in alloy 625 using ultrasonic waves and correlation with tensile properties. Scripta Mater 2001;45:1025–30.

[21] Albuquerque VHC, Silva EM, Leite JP, Moura EP, Freitas VLA, Tavares JMRS. Spinodal decomposition mechanism study on the duplex stainless steel UNS S31803 using ultrasonic speed measurements. Mater Des 2010;31: 2147–50.

[22] Silva EM, Albuquerque VHC, Leite JP, Varela ACG, Moura EP, Tavares JMRS. Phase transformations evaluation on a UNS S31803 duplex stainless steel based on nondestructive testing. Mater Sci Eng A 2009;516:126–30.

[23] Normando PG, Moura EP, Souza JA, Tavares SSM, Padovese LR. Ultrasound, eddy current and magnetic Barkhausen noise as tools for sigma phase detection on a UNS S31803 duplex stainless steel. Mater Sci Eng A 2010;527:2886–91.

[24] Shankar V, Rao KBS, Mannan SL. Microstructural and mechanical properties of Inconel 625 superalloy. J Nucl Mater 2001;288:222–32.

[25] ASNT 147/147WCD, Nondestructive Testing Handbook, 3rd ed., vol. 7, Ultrasonic Testing, American Society for Nondestructive Testing; 2007.

[26] Vieira AP, Moura EP, Gonçalves LL, Rebello JMA. Characterization of welding defects by fractal analysis of ultrasonic signals. Chaos Soliton Fract 2008;38:748–54.

[27] Moura EP, Souto CR, Silva AA, Irmão MAS. Evaluation of principal component analysis and neural network performance for bearing fault diagnosis from vibration signal processed by RS and DF analyses. Mech Syst Signal Process 2011;25:1765–72.

[28] Hurst HE. Long-term storage capacity of reservoirs. Trans Am Soc Civil Eng 1951;116:770–99.

[29] Peng CK, Buldyrev V, Havlin S, Simmons M, Stanley HE, Goldberger AL. Mosaic organization of DNA nucleotides. Phys Rev E 1994;49:1685–9.

[30] Webb R. Statistical Pattern Recognition. 2nd ed. West Sussex, UK: John Wiley & Sons; 2002.

[31] Silva CC, Afonso CRM, Miranda HC, Ramirez AJ, Farias JP. Microstructure of Alloy 625 Weld Overlay. AWS Fabtech Conference, Chicago, IL, USA; 2011.

[32] Silva CC, Miranda HC, Farias JP, Afonso CRM, Ramirez AJ. Carbide/Nitride Complex Precipitation – An Evaluation by Analytical Electron Microscopy. In: 17th International Microscopy Congress, Rio de Janeiro, Brazil, 2010.

[33] Kumar A, Shankar V, Jayakumar T, Rao KBS, Raj B. Effect of precipitates on the correlation of ultrasonic velocity with mechanical properties in Ni-based superalloy Inconel 625. In: European conference on nondestructive testing, Barcelona, Spain, 2002.

[34] Shull PJ. Nondestructive evaluation-theory, techniques and applications. 1st ed. New York, USA: Marcel Dekker; 2009.

[35] Kim SA, Johnson WL. Elastic constants and internal friction of martensitic steel, ferritic-pearlitic steel, and α-iron. Mater Sci Eng A 2007;452–453:633–9.

[36] Freitas VLA, Albuquerque VHC, Silva EM, Silva AA, Tavares JMRS. Nondestructive characterization of microstructures and determination of elastic properties in plain carbon steel using ultrasonic measurements. Mater Sci Eng A 2010;527:4431–7.

[37] Freitas VLA, Normando PG, Albuquerque VHC, Silva EM, Silva AA, Tavares JMRS. Nondestructive characterization and evaluation of embrittlement kinetics and elastic constants of duplex stainless steel SAF 2205 for different aging times at 425 °C and 475 °C. J Nondestruct Eval 2011;30:130–6.

[38] Albuquerque VHC, Melo TAA, Oliveira DF, Gomes RM, Tavares JMRS. Evaluation of grain refiners influence on the mechanical properties in a CuAlBe shape memory alloy by ultrasonic and mechanical tensile testing. Mater Des 2010;31:3275–81.

[39] Krüger SE, Rebello JMA. Hydrogen damage detection by ultrasonic spectral analysis. NDT E Int 1999;32:275–81.

[40] Guo N, Lim MK, Pialucha T. Measurement of attenuation using a normalized amplitude spectrum. J Nondestruct Eval 1995;14:9–19.

[41] Bouda AB, Benchaala A, Alem K. Ultrasonic characterization of materials hardness. Ultrasonics 2000;38:224–7.

[42] Bouda AB, Lebaili S, Benchaala A. Grain size influence on ultrasonic velocities and attenuation. NDT E Int 2003;36:1–5.

[43] Kohavi R, Provost F. Glossary of terms. Mach Learn 1998;30:271–4.